

Axisymmetric gravity currents in a rotating system: experimental and numerical investigations

By MARK A. HALLWORTH¹, HERBERT E. HUPPERT¹
AND MARIUS UNGARISH²

¹Institute of Theoretical Geophysics, Department of Applied Mathematics and Theoretical Physics, Silver Street, Cambridge CB3 9EW, UK

²Department of Computer Science, Technion, Haifa 32000, Israel

(Received 2 June 2000 and in revised form 24 January 2001)

The propagation at high Reynolds number of a heavy, axisymmetric gravity current of given initial volume over a horizontal boundary is considered in both rotating and non-rotating situations. The investigation combines experiments with theoretical predictions by both shallow-water approximations and numerical solutions of the full axisymmetric equations. Attention is focused on cases when the initial ratio of Coriolis to inertia forces is small. The experiments were performed by quickly releasing a known cylindrical volume of dense salt water of 2 m diameter at the centre of a circular tank of diameter 13 m containing fresh ambient water of typical depth 80 cm. The propagation of the current was recorded for different initial values of the salt concentration, the volume of released fluid, the ratio of the initial height of the current to the ambient depth, and the rate of rotation. A major feature of the rotating currents was the attainment of a maximum radius of propagation. Thereafter a contraction–relaxation motion of the body of fluid and a regular series of outwardly propagating pulses was observed. The frequency of these pulses is slightly higher than inertial, and the amplitude is of the order of magnitude of half the maximum radius. Theoretical predictions of the corresponding gravity currents were also obtained by (i) previously developed shallow-water approximations (Ungarish & Huppert 1998) and (ii) a specially developed finite-difference code based on the full axisymmetric Navier–Stokes equations. The ‘numerical experiments’ provided by this code are needed to capture details of the flow field (such as the non-smooth shape of the interface, the vertical dependence of the velocity field) which are not reproduced by the shallow-water model and are very difficult for, or outside the range of, accurate experimental measurement. The comparisons and discussion provide insight into the flow field and indicate the advantages and limitations of the verified simulation tools.

1. Introduction

The lateral spread of fluid of one density into fluid of a different density forms an important class of well-known fluid flows termed gravity currents. The driving force behind such flows is provided by the density contrast between the fluids, which may arise through thermal and/or compositional differences, and is a ubiquitous feature of many natural and man-made situations, as reviewed by Simpson (1997) and Huppert (2000).

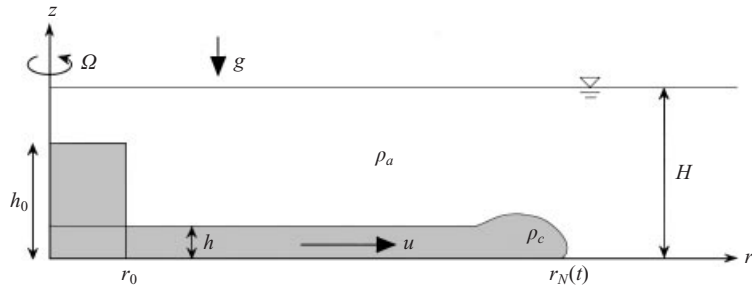


FIGURE 1. A sketch of the configuration of the system.

Since gravity currents play such a fundamental role in the circulation of the atmosphere and hydrosphere over a large range of scales and geometric configurations, their behaviour has been widely investigated by laboratory experiments and a variety of theoretical models. One area of research, of particular relevance to large-scale environmental gravity currents, is the influence of Coriolis forces exerted by the Earth's rotation. On a smaller scale, the deliberate (and generally more rapid) rotation of fluids in certain industrial situations can have either advantageous or detrimental consequences for the desired process, and their design may benefit from an improved understanding of rotation effects.

The present paper concentrates on the axisymmetric spreading of dense currents over a rigid, horizontal floor, and deals specifically with how the behaviour of such flows is modified by the effects of rotation. This work forms a direct extension to the theoretical description of the same system using inviscid shallow-water equations presented by Ungarish & Huppert (1998, hereafter referred to as UH), to which the reader is referred for a more comprehensive introduction.

The new material presented here includes the results of a series of laboratory experiments and theoretical predictions based on finite-difference numerical solutions of the full axisymmetric equations, both of which are compared with the previously obtained results using the shallow-water approximation.

The system under consideration is depicted schematically in figure 1. A layer of ambient fluid, of constant density ρ_a , above a solid horizontal surface at $z = 0$, is in solid body rotation with angular velocity Ω about a vertical axis of symmetry z . At time $t = 0$, a fixed volume of co-rotating denser fluid of density ρ_c , initially contained in a cylinder of height h_0 and radius r_0 , is instantaneously released into the ambient fluid, generating a radially spreading rotating gravity current.

We use a cylindrical coordinate system rotating with angular velocity Ω about the vertical axis z with a gravitational acceleration of $-g\hat{z}$. The velocity vector is denoted by $\mathbf{v} = u\hat{r} + v\hat{\theta} + w\hat{z}$ in terms of the unit vectors $\hat{r}, \hat{\theta}, \hat{z}$ in the radial, azimuthal and axial directions respectively. The angular velocity in the rotating system is denoted by $\Omega = v/r$. The driving force is the reduced gravity defined by

$$g' = \epsilon g, \quad (1.1)$$

where

$$\epsilon = (\rho_c - \rho_a)/\rho_a. \quad (1.2)$$

We are concerned with predicting the behaviour of the current after release, in particular the radius of propagation, $r_N(t)$, the shape of the interface separating heavy and ambient fluid, $h(r, t)$, and the profiles of the radial and angular velocity. To

facilitate the theoretical description we assume that the flow is axially symmetric, incompressible and laminar. We concentrate on situations in which the rotational effects are initially small (the ratio of Coriolis to inertia terms, represented by the parameter $\bar{\mathcal{C}}$ defined below, is small); in the opposite case very little propagation occurs and no proper current actually appears. Viscous effects, represented by the inverse of the Reynolds number defined below, are similarly small.

The investigated configuration contains several special features. First, we emphasize that the axisymmetric current, even without rotation, is more complicated and less understood than its rectangular (usually assumed two-dimensional) equivalent. Second, in a rotating system the counter-intuitive Coriolis-centrifugal forces affect the flow and hinder the propagation. This produces some features without counterpart in non-rotating circumstances, such as the existence of a maximum radius, inverse motion, and (quasi-) steady-state lens structures. These features are not as yet well understood or even documented. The objective of this work is to elucidate these issues by using both large-scale experimental and numerical methods.

1.1. The shallow-water (SW) inviscid formulation

Previous investigations of this problem based on the shallow-water inviscid approximation have proved to be extremely versatile in the analysis of gravity currents in various circumstances. A brief review for the present case, following that formulated for rotating, axisymmetric currents by UH, is as follows.

The following main simplifications are introduced. A sharp interface is assumed to divide the current of fixed volume and constant density ρ_c and the ambient fluid of constant density ρ_a . The current domain, $0 \leq r \leq r_N$, $0 \leq z \leq h(r, t)$, is assumed ‘shallow’ (i.e. the ratio of radial to vertical scales $r_N/h \gg 1$), and the flow inside is typified by a large Reynolds (also Grashof) number as defined below and amenable to the Boussinesq approximation (i.e. $\epsilon \ll 1$). Consistent with these simplifications, in the one-layer version used here it is further assumed that the ambient fluid is relatively very deep, within which $u = v = w = 0$, and hence the pressure P is hydrostatic and expressed as

$$P = \rho_a(\frac{1}{2}\Omega^2 r^2 - gz) + P_0 \quad (z \geq h(r, t)), \quad (1.3)$$

for some constant P_0 .

In the dense fluid domain, the vertical force balance is also (almost) hydrostatic, and hence the pressure continuity with (1.3) on the interface defines the connection between P and h :

$$\frac{\partial P}{\partial r} = \rho_a \Omega^2 r + \rho_a g' \frac{\partial h}{\partial r} \quad (z \leq h(r, t)). \quad (1.4)$$

We now take the z -average of the continuity, radial and azimuthal momentum equations, see (3.2)–(3.3), and eliminate the pressure using (1.4). Letting \mathcal{U}, \mathcal{V} be the z -averaged representative velocity variables, which are functions of r and t , we obtain the approximate *dimensionless* governing hyperbolic system given by:

the equation of continuity,

$$\frac{\partial h}{\partial t} + \frac{\partial}{\partial r} \mathcal{U} h = -\frac{\mathcal{U} h}{r}; \quad (1.5)$$

the equation of radial momentum,

$$\frac{\partial}{\partial t} \mathcal{U} h + \frac{\partial}{\partial r} [\mathcal{U}^2 h + \frac{1}{2} h^2] = -\frac{\mathcal{U}^2 h}{r} + \bar{\mathcal{C}}^2 \mathcal{V} h \left(2 + \frac{\mathcal{V}}{r} \right); \quad (1.6)$$

and the equation of azimuthal momentum

$$\frac{\partial}{\partial t} \mathcal{V}h + \frac{\partial}{\partial r} \mathcal{U}\mathcal{V}h = -2\mathcal{U}h \left(1 + \frac{\mathcal{V}}{r} \right); \quad (1.7)$$

for the variables of h (height) and \mathcal{U}, \mathcal{V} (z -averaged velocities) in the current domain. The convenient scaling used for these equations, as discussed by Ungarish & Huppert (1999), is to non-dimensionalize r with r_0 , z with h_0 , time with $r_0/(g'h_0)^{1/2}$, \mathcal{U} with $(h_0g')^{1/2}$ and \mathcal{V} with Ωr_0 . In this case the dimensionless parameters that enter the problem are

$$\bar{\mathcal{C}} = \frac{\Omega r_0}{(h_0g')^{1/2}}, \quad (1.8)$$

which expresses the ratio of Coriolis to inertia effects (the inverse of a Rossby number), and the ratio of the ambient depth, H , to the initial height of the dense fluid, h_0 . The viscous terms have been neglected, and therefore the initial representative Reynolds number,

$$Re_0 = h_0(h_0g')^{1/2}/\nu, \quad (1.9)$$

where ν is the kinematic viscosity of the dense fluid, is assumed to be very large and hence does not appear in this formulation. The initial conditions are simply

$$r_N = 1, \quad h = 1, \quad \mathcal{U} = \mathcal{V} = 0 \quad \text{and } H \text{ given } (t = 0). \quad (1.10)$$

Boundary conditions for the velocities are necessary at $r = 0$ and $r = r_N(t)$. At the former position $\mathcal{U} = \mathcal{V} = 0$. Potential vorticity conservation provides, at $r = r_N$,

$$\omega(r_N, t) = -1 + [1/r_N(t)]^2, \quad (1.11)$$

where $\omega = \mathcal{V}/r$. In addition, to close the formulation, the semi-empirical Froude condition for \mathcal{U} at the nose (whose position is indicated by the subscript N) must be introduced. The works of Benjamin (1968), Huppert & Simpson (1980), Härtel, Meiburg & Necker (2000) and others indicate that, in our non-dimensional form, at the ‘nose’ of a *rectangular* current the velocity of propagation is related to the height by

$$\frac{dr_N}{dt} = Fr \times h_N^{1/2}, \quad (1.12)$$

where the Froude number Fr is given approximately by (Huppert & Simpson 1980)

$$Fr = \begin{cases} 1.19 & (h_N/H \leq 0.075) \\ 0.5(H/h_N)^{1/3} & (0.075 \leq h_N/H \leq 1). \end{cases} \quad (1.13)$$

A straightforward extension is to use (1.13) for the axisymmetric current. Moreover, UH argued that (1.13) is also valid in a rotating frame (for $\bar{\mathcal{C}} \ll 1$ at least). The use of this Froude condition conveniently closes the SW inviscid single-layer formulation, but it must be emphasized that there is no clear-cut justification for this step. One of the objectives of the present investigation is the verification of this postulate.

The solution of the time-dependent SW equations is in general obtained numerically (by a finite-difference Lax–Wendroff scheme or similar methods). For a quick analysis, some approximate solutions by asymptotic expansions for small values of $\bar{\mathcal{C}}$, and by ‘box-model’ (momentum-integral methods) are also available; details are given in UH, Ungarish & Huppert (1999), Hogg, Ungarish & Huppert (2001) and others.

For the rotating case ($\bar{\mathcal{C}} > 0$) the foregoing SW equations admit a non-trivial steady-state solution: the dense fluid has a steady-lens shape, with no internal radial

motion ($\mathcal{U} = 0$), and the external pressure forcing is balanced by centrifugal-Coriolis internal accelerations sustained by a retrograde azimuthal motion. The steady-lens structures have been analysed by Flierl (1979), Csanady (1979), Griffiths & Linden (1981), Choboter & Swaters (2000) and others referenced therein, mostly with regard to their stability. The pertinent (approximate) results can be simply expressed as

$$r_N = 2^{1/2}\bar{\mathcal{C}}^{-1/2}, \quad \omega = -1 + \bar{\mathcal{C}}[1 - (1 - \frac{1}{2}y^2)], \quad h = \bar{\mathcal{C}}(1 - y^2), \quad (1.14)$$

for $\bar{\mathcal{C}} \ll 1$, and

$$r_N = 1 + \frac{1}{2\bar{\mathcal{C}}}, \quad \omega = -\frac{1}{\bar{\mathcal{C}}} \exp[2\bar{\mathcal{C}}(y - 1)], \quad h = 1 - \exp[2\bar{\mathcal{C}}(y - 1)], \quad (1.15)$$

for $\bar{\mathcal{C}} \gg 1$, where $y = r/r_N$ ($0 \leq y \leq 1$). Recall that r_N, h and ω are scaled with the initial radius, initial height and angular velocity of the system, respectively. The dimensional length $r_0/(2\bar{\mathcal{C}})$ is defined as the Rossby radius of deformation. In the large- $\bar{\mathcal{C}}$ (small Rossby number) case this is indeed the deformation of the lens with respect to the initial radius, and is relatively small. On the other hand, in the case of small $\bar{\mathcal{C}}$ the deformation of the steady lens with respect to the initial radius is large, but still much smaller than the Rossby radius of deformation.

The SW results indicate remarkable differences between non-rotating and rotating gravity currents even for ‘weak’ rotation (small $\bar{\mathcal{C}}$). A non-rotating inviscid current quickly acquires a nose-up tail-down shape and spreads to infinity. In the rotating case (with small $\bar{\mathcal{C}}$) the propagation starts as in the non-rotating counterpart, but after about one tenth of a revolution of the system the nose is pushed down by Coriolis effects, and the dense-fluid domain tends towards a lens shape. A maximum radius of propagation, r_{\max} , is reached in less than one half-revolution of the system. The angular velocity lag in the current is large (ω is close to -1). However, the connection between the propagating current and the steady lens result is not evident; the maximal radius exceeds by about 35% the steady lens radius, after which the available SW formulation becomes unreliable. We note in passing that the ‘box model’ estimate (Ungarish & Huppert 1999) of the maximum radius is given by

$$r_{\max} \approx 1.6\bar{\mathcal{C}}^{-1/2} \quad (\bar{\mathcal{C}} \ll 1). \quad (1.16)$$

The SW analysis has several advantageous features: the computations are relatively easy, some analytical investigations are possible, and it admits extensions to various circumstances, such as to a permeable lower boundary. Most important, the predictions of $r_N(t)$ turn out to be in fair agreement with experiments. On the other hand, this formulation (in its present form, at least) also contains some intrinsic deficiencies: the accuracy of the approximations is not clearly known, the ‘nose condition’ requires verification, and only idealized initial conditions can be considered. Perhaps the most important limitation is the fact that many details of the flow field cannot be captured by this simplified model. Some of the neglected effects (the Ekman layers, the reverse flow, the friction at the interface between the current and the ambient) are expected to become important at certain stages.

Experimental investigations of this problem are also scarce. The flow in the non-rotating axisymmetric case can be conveniently visualized in a wedge-shaped container (Simpson 1997; Huq 1996). The influence of the friction on the sidewalls in such configurations is, however, not well understood. For example, in Huq’s experiments the initial speed of propagation was substantially larger than the theoretical predictions for a truly axisymmetric case, and the reason for the discrepancy is not known. On the other hand, experiments in a rotating frame must be performed in cylindrical tanks

and direct observation of the (r, z) -plane is difficult. UH performed some rotating experiments in a tank of 90 cm diameter containing fresh water, with an inner cylinder (lock) of 9.4 cm diameter initially containing saltwater to a height of 15 cm. Typical values of g' and Ω were 50 cm s^{-2} and 0.3 s^{-1} respectively. The measured values of $r_N(t)$ were in fair agreement with the SW theory, but many details could not be observed in this geometry. In particular, the thickness of the current decreased quickly ($\approx 5 \text{ s}$) to about 1 cm, which both hindered observation and invoked viscous influence from the Ekman layers which were of similar thickness.

A solid body of experimental data and more sophisticated theoretical formulations are needed, and so the objective of the present investigation is to throw more light on the problem by analysing data from large-scale experiments in conjunction with evaluating numerical solutions of the ‘full’ equations of motion. Such numerical solutions have been attempted for gravity currents, e.g. by Wang (1985) and recently by Härtel *et al.* (1999) – but in very different geometries and parameter ranges; to our best knowledge, no such attempt has been made for the present problem. Comparisons of the present results with predictions of the SW approximations are also performed and discussed.

The paper is organized as follows. The new experiments and a discussion of the results are presented in §2. In §3 the finite-difference code is described and some results, closely connected with the experimental data, are presented and discussed. Some concluding remarks are given in §4.

2. Experiments

2.1. Experimental set-up and procedure

The experiments were conducted in the Coriolis laboratory at the Laboratoire des Ecoulements Géophysiques et Industriels, Grenoble. The Coriolis turntable is a 14 m diameter circular platform capable of rotating about a vertical axis with a period of between 18 and 1000 s, with an accuracy of the rotation rate $d\Omega/\Omega$ of 10^{-4} . The table is equipped with a 13.0 m diameter, 1.2 m deep circular tank, which may be filled with freshwater or brine supplied from large mixing tanks.

All the experiments reported here involved lock-release gravity currents in which fixed volumes of dense saltwater, initially held behind a central 1 m high cylindrical lock of radius 1 m, were allowed to intrude into freshwater surroundings following the rapid vertical removal of the lock. A sketch of the experimental configuration is presented in figure 2. The lock was specially designed and constructed for these experiments from a cylinder of lightweight plastic strengthened by four horizontal steel hoops. The lock could be raised and lowered by means of a pulley system connecting the uppermost hoop to a manually operated winding spool by four steel cables. In order to prevent tilting or lateral motion, the lift was guided by four thin vertical rods fixed 90° apart on the floor of the tank, and positioned in contact with sliding runners secured to the inner wall of the lock cylinder. The basal edge of the lock was seated on a 1 cm thick foam sealing ring on the tank floor.

The experimental procedure began by filling the entire tank with fresh water to the desired depth. A vernier screw gauge mounted on the perimeter wall allowed the height of the free surface at the wall H_w to be measured to within $\pm 0.5 \text{ mm}$. Once the lock cylinder had been lowered and sealed on the tank floor, a known volume of red-dyed saltwater was then slowly fed into the base of the lock beneath a circular plate fixed 1 cm above the floor, designed to minimize mixing with ambient

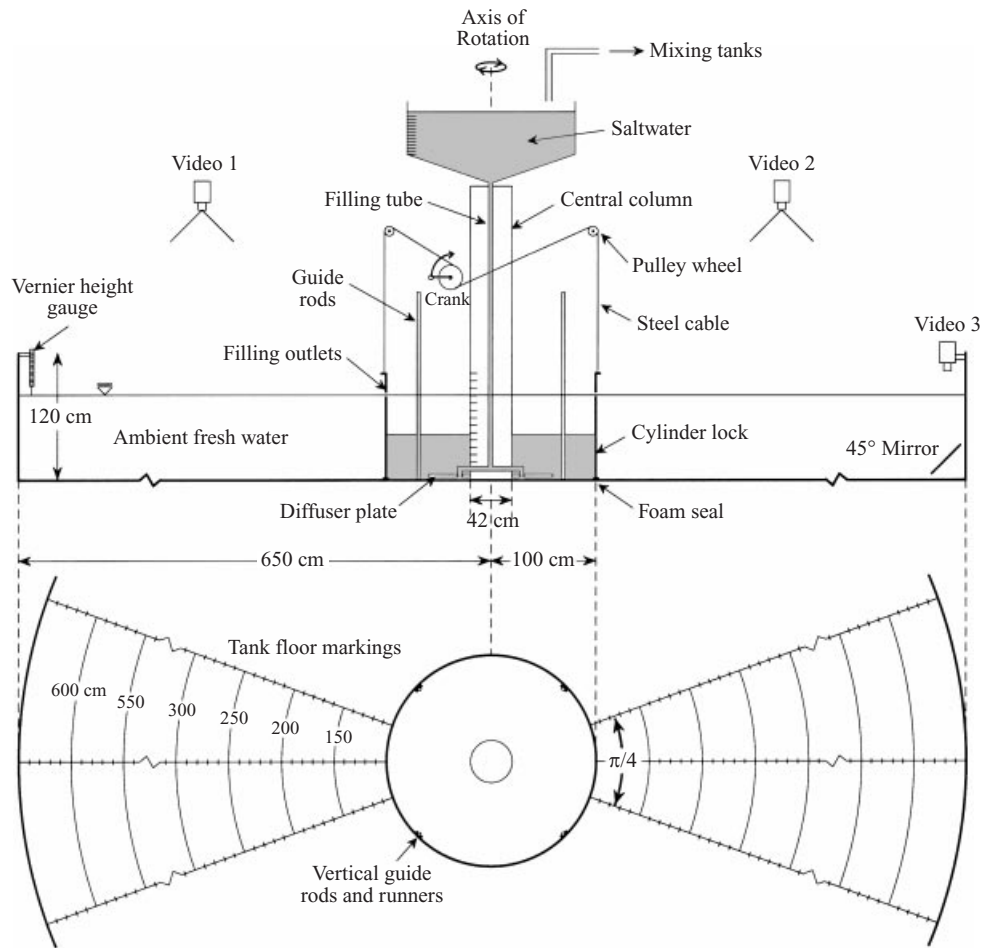


FIGURE 2. Elevation and plan schematic of the experimental tank.

fluid upon entry. A sharp, stable interface separating the incoming saltwater from the overlying fresh ambient inside the lock was thus formed, which slowly rose as the filling proceeded until the desired height was reached. The ambient fluid displaced during the filling of the lock escaped through a number of 1 cm diameter holes arranged around the perimeter of the lock wall at the height of the free surface. On completion of the filling, the final height, h_0 , of the saltwater interface was read off a graduated scale on the central column at a radius of $r_i = 21$ cm, and the densities of both the saltwater and ambient freshwater were measured by hydrometers accurate to within $\pm 0.0001 \text{ g cm}^{-3}$.

Each experiment was started by rapid vertical lifting of the lock cylinder. The vertical travel required was achieved after approximately 2.5 manual revolutions of the crank handle, which could be smoothly and reproducibly completed within about 6 s. In practice, the base of the lock was raised to a height 1 cm below the free surface, since complete clearance would have generated unwanted surface disturbances. Upon release, the ensuing gravity current was observed to spread radially across the floor of the tank. The flow was recorded by two overhead video cameras covering diametrically opposite sectors of angular width $\pi/4$ marked on the tank floor. Each sector was

Expt	Ω (s^{-1})	h_0 (cm)	H (cm)	h_0/H	V_0 (m^3)	ρ_c (g cm^{-3})	ρ_a (g cm^{-3})	g' (cm s^{-2})	$\bar{\mathcal{C}}^2$	Re_0 ($\times 10^5$)	r_{\max} (cm)	ω_p (s^{-1})
(a) Non-rotating currents												
S1	0	41.1	50.10	0.820	1.234	1.0045	0.9995	4.91	0	0.59	–	–
S2	0	77.3	80.10	0.965	2.321	1.0042	0.9993	4.81	0	1.52	–	–
S3	0	45.8	79.80	0.574	1.375	1.0192	0.9996	19.24	0	1.36	–	–
S7	0	45.2	80.00	0.565	1.357	1.0441	0.9995	43.77	0	2.01	–	–
(b) Rotating currents												
R4	0.0500	46.4	80.27	0.578	1.393	1.0192	0.9996	19.24	0.0282	1.37	550	0.100
R10	0.0500	46.3	79.97	0.579	1.390	1.0107	1.0007	9.80	0.0551	0.99	450	0.102
R12	0.0500	47.0	82.92	0.567	1.411	1.0107	1.0011	9.41	0.0565	0.99	450	0.111
R13	0.0500	47.0	80.03	0.587	1.411	1.0094	0.9995	9.72	0.0514	1.10	–	–
R14	0.0500	44.0	81.12	0.524	1.321	1.0094	0.9995	9.72	0.0585	0.91	–	–
R11	0.0641	77.0	81.64	0.943	2.312	1.0107	1.0009	9.61	0.0556	2.09	420	0.140
R15	0.0775	46.7	81.67	0.572	1.402	1.0242	0.9996	24.14	0.0533	1.57	450	0.165
R16	0.0775	16.7	82.07	0.203	0.500	1.0242	0.9998	23.94	0.1502	0.39	330	0.165
R17	0.0775	48.0	83.17	0.577	1.441	1.0242	0.9998	23.94	0.0523	1.63	440	0.165
R5	0.1000	46.6	80.10	0.582	1.399	1.0192	0.9998	19.04	0.1135	1.37	370	0.207
R6	0.1000	77.0	81.00	0.951	2.312	1.0194	1.0000	19.03	0.0685	2.93	400	0.207
R8	0.1000	46.1	79.90	0.577	1.384	1.0438	0.9999	43.07	0.0504	2.05	470	0.207
R9	0.1500	46.2	79.51	0.581	1.387	1.0436	1.0004	42.36	0.1149	2.04	370	0.314

TABLE 1. Initial conditions of the axisymmetric lock-release gravity currents in (a) non-rotating and (b) rotating systems. In all cases $r_0 = 100$ cm. Also shown are the experimentally determined values of the maximum radius attained by the first radially propagating front and the frequency of the subsequent fronts for the rotating currents, ω_p . $\bar{\mathcal{C}}$ and Re_0 are defined by (1.8) and (1.9).

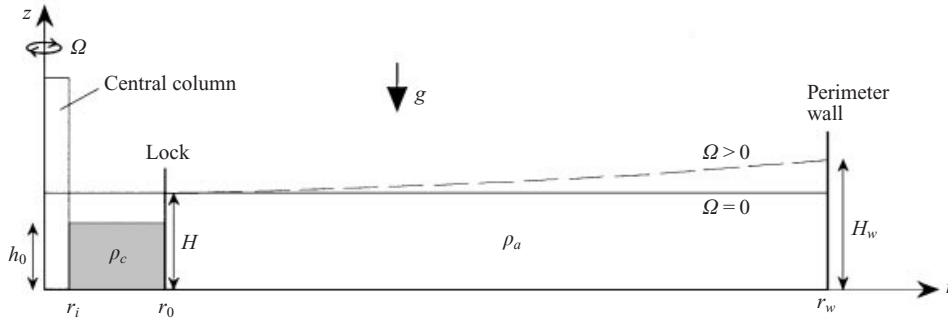


FIGURE 3. The initial configurations of lock-release gravity currents. An exaggerated view of the parabolic bending of the free surface due to rotation is shown as a dashed line to illustrate the variation in initial height at different radii.

marked with concentric arcs with radial spacings of 50 cm, in addition to 10 cm graduations along three radial lines (see figure 2). The rates of radial propagation of the currents were measured by subsequent analysis of the video recordings to determine the average time of arrival of the current front at fixed distances along all six radial lines. A third video camera was mounted on the perimeter wall of the tank above a submerged 45° mirror to record a vertical profile of the current along a radius. This view was illuminated by a vertical laser sheet in the plane of three vertical scale bars at fixed radii of 200, 250 300 cm, and relied on either red dye or fluorescein to delimit the current profile.

A total of 17 experiments were conducted, exploring various combinations of initial conditions of the relevant parameters, namely the rate of rotation Ω , the ambient depth H , the initial height of the current h_0 (and hence $V_0 = \pi h_0(r_0^2 - r_i^2)$, where r_0 , the radius of the lock, and r_i , the radius of the central column, were always fixed at 100 cm and 21 cm respectively), and the reduced gravity $g' = g(\rho_c - \rho_a)/\rho_a$. A full listing of the initial experimental conditions is given in table 1. Four experiments (prefixed by the letter S) were performed with no rotation. The remaining thirteen experiments (prefixed by the letter R) were conducted with rotation rates varying between 0.05 and 0.15 s^{-1} .

The viscous effects were expected to be small. The initial Reynolds number in all experiments was typically 10^5 . Continuity indicates that h decays like r_N^{-2} and therefore the effective Reynolds number, which is proportional to $h^{3/2}$, see (1.9), is expected to decrease like r_N^{-3} . According to this estimate, the Reynolds number decays to about 360 when the current reaches $r_N = 6.5$ (the dimensionless outer radius of the tank). The accompanying Ekman number, $\nu/(\Omega h^2)$, which expresses the ratio of viscous to Coriolis forces in the rotating current, varied typically from 10^{-4} at release to 10^{-2} at maximal propagation. (The Ekman boundary-layer length scale $(\nu/\Omega)^{1/2}$ was 0.45 cm in the cases with the slowest rate of rotation.)

2.2. Results for non-rotating currents

A sketch of the initial configuration is shown in figure 3. Each release generated an almost perfectly axisymmetric density current which spread radially across the floor of the tank. In profile, the current adopted the characteristic shape of a raised, bulbous head advancing in front of a much thinner tail region. In all the runs reported here, the flows reached the perimeter wall, whereupon they were reflected and observed to propagate back towards the centre of the tank. The position of the front of the

current r_N as a function of time t for all four non-rotating currents prior to reflection off the perimeter wall is plotted in figure 4(a). The data show a decrease in the velocity of the front with increasing radius (or time), and agree very well with the solutions of the SW model approximation (plotted as solid curves in figure 4a). For experiments S1 and S2 the discrepancy is within the range of the experimental errors. For S3 and S7 the SW propagation rate is systematically faster than the experimental value. This discrepancy can be attributed to the delay introduced by the manual lifting of the lock cylinder, which is not incorporated in the theory. For S1 and S2 the typical velocities of propagation are smaller than those of S3 and S7, and consequently the former are less influenced by the lock removal than the latter.

With the compensation for the lock removal effect in mind, we infer that the SW theory provides a very good prediction of $r_N(t)$ for an instantaneous release of an axisymmetric current in the parameter range tested by the experiments. This conclusion strongly validates the use of the nose condition (1.12)–(1.13) for axisymmetric currents. It is remarkable that the SW model used here is of a single-layer type, and information about the finite depth of the ambient layer is entirely contained in the value of H/h_N which enters the correlation (1.13).

The most simple theoretical treatment of non-rotating axisymmetric gravity currents is the so-called ‘box-model’ approach developed by Huppert & Simpson (1980), in which the current is assumed to spread as a series of equal-volume cylinders, and for the $Fr = 1.19$ case leads to an expression for the radial propagation as a function of time given by

$$r = 1.16(g'V_0)^{1/4}t^{1/2}. \quad (2.17)$$

Dimensional analysis suggests defining suitable scaling parameters for r and t as $r_* = V_0^{1/3}$ and $t_* = (g'^3/V_0)^{-1/6}$ respectively, in which case the dimensionless form of (2.17) can be written as

$$R = 1.16T^{1/2}, \quad (2.18)$$

where $R = r/r_*$ and $T = t/t_*$. The scaled experimental data and theoretical curve given by (2.18) are plotted in figure 4(b), which shows a satisfactory collapse of the data beyond the slumping distance of between 3 and 4 lock radii, as explained by Huppert & Simpson (1980), and Hallworth *et al.* (1996).

2.3. Rotating currents

A sketch of the initial configuration is shown in figure 3. For each experiment, all the contained fluid was in solid body rotation prior to release of the gravity current, which was achieved by spinning up the system for about three hours before each run (the typical spin-up time scale, $H/(v\Omega)^{1/2}$, was less than 50 min). The rotation caused a small parabolic bending of the free surface. The value of H given in table 1, which we consider as the representative height of the free surface, is the initial height at the radius of the lock calculated by

$$H = H_w - \frac{\Omega^2(r_w^2 - r_0^2)}{2g}, \quad (2.19)$$

where H_w was the experimentally measured free surface height at $r_w = 650$ cm.

Upon release from the lock, the initial behaviour of the rotating currents was very similar to that in a non-rotating system, with a decelerating front spreading radially across the floor of the tank. Beyond a certain radius, however, the deceleration became noticeably more pronounced than for the equivalent non-rotating currents. Overall, the propagation appeared nicely axisymmetric. Locally, however, the leading edge

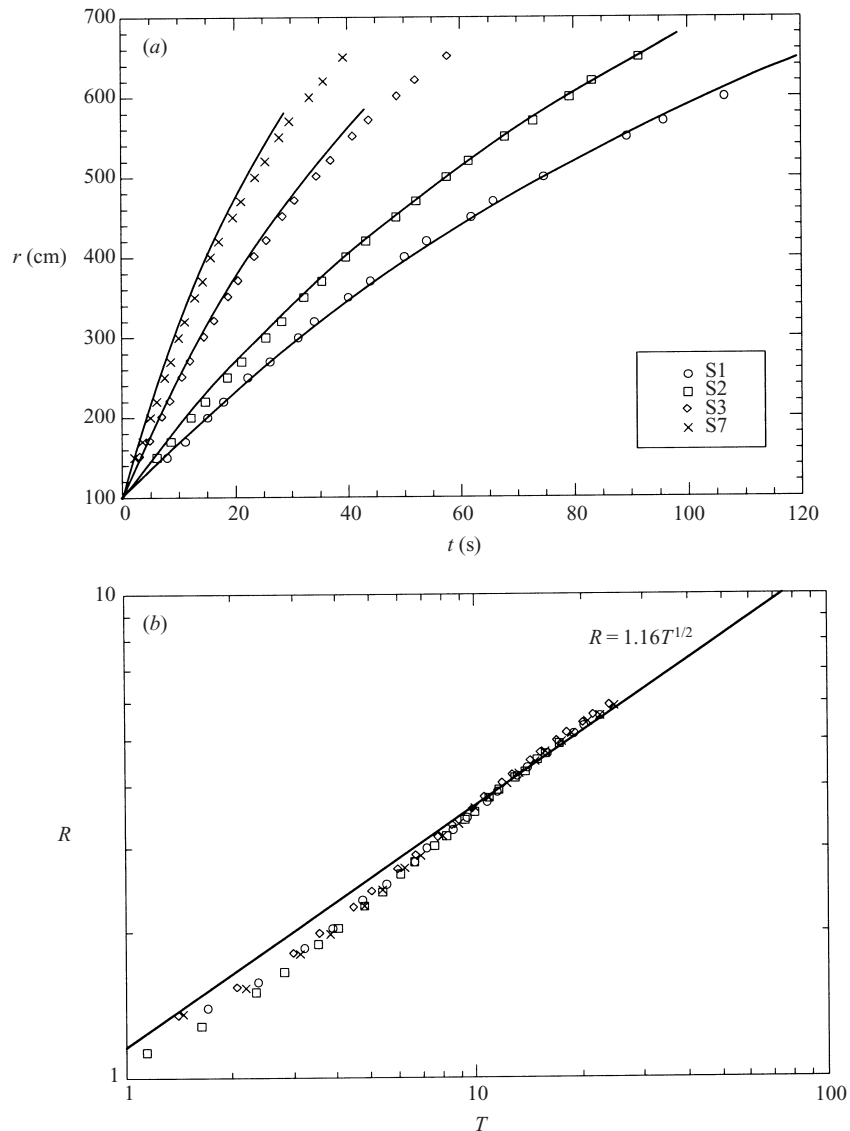


FIGURE 4. Non-rotating flows. (a) The radius of the front of the current as a function of time. The experimental data (symbols) are compared with the corresponding SW prediction (lines). (b) The collapse of the dimensionless data and the corresponding theoretical ‘box model’ relationship (2.18).

displayed some instabilities. The measured values of the propagation as a function of time are displayed in figure 5, accompanied, again, by the SW model results. A noticeable effect is that, as opposed to the non-rotating cases, none of the rotating currents reached the outer wall of the tank. Evidently, at a certain radius defined here as r_{\max} , the forward motion at the front ceased, at which point the height of the current was extremely thin. The SW model predictions of $r_N(t)$ are in fair agreement with the experimental points until the maximum radius is attained (at $\Omega t \approx 2$ according to the SW model). Afterwards, the SW theory predicts a contraction.

Remarkably, for a period several seconds prior to the arrest of the initial leading edge, a reverse flow in the ensuing tail was evident, and the bulk volume of the

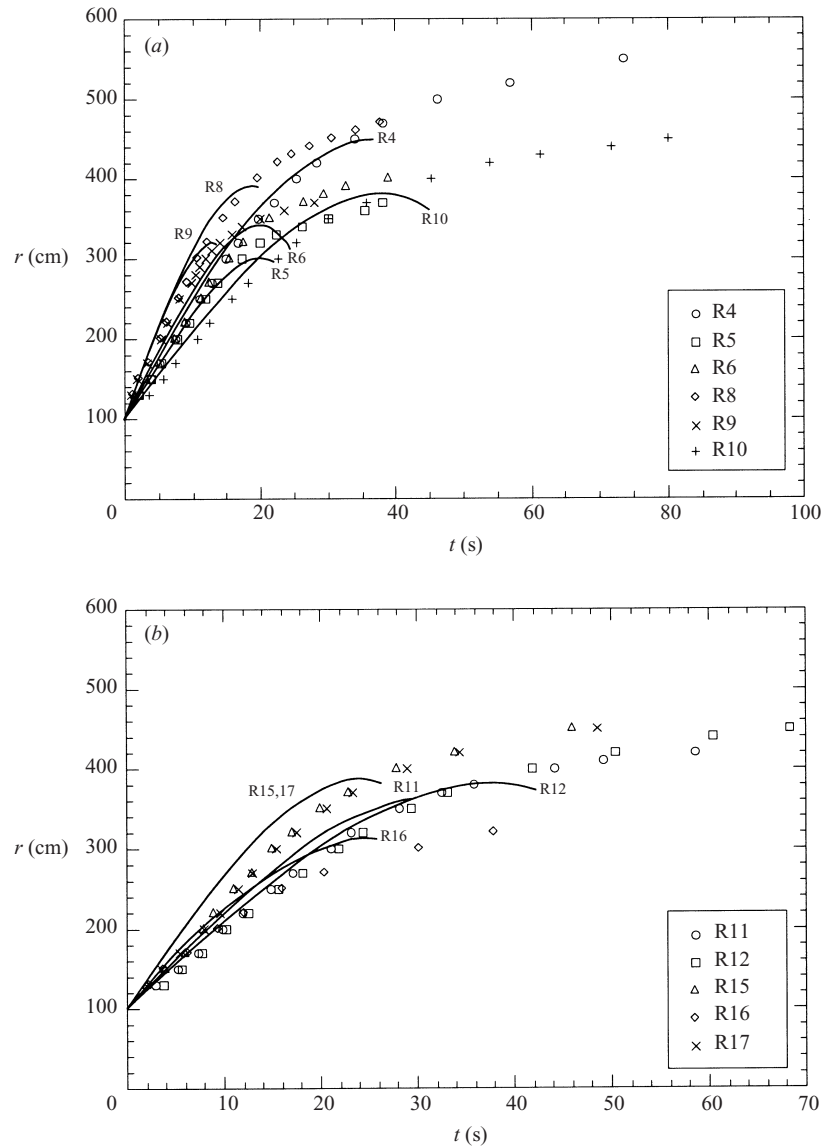


FIGURE 5. Rotating flows. The radius of the first outwardly propagating front of the current as a function of time. The experimental data (symbols) are compared with the corresponding SW model predictions (lines).

current contracted and increased in thickness back towards the centre of the tank. Thereafter, this newly accumulated central body of fluid relaxed and generated a second outwardly propagating pulse of fluid with a clearly defined leading edge that reached and slightly exceeded the previous arrest radius at r_{\max} . This behaviour was repeated several times, and at least five discrete contractions followed by outward pulses were observed in each experiment. The radius of the initial front, and the leading edge of subsequent pulses is plotted as a function of time in figure 6. Analyses of these plots enables a mean pulse period T_p to be determined for each experiment, defined as the averaged time interval between the arrival of successive fronts at any

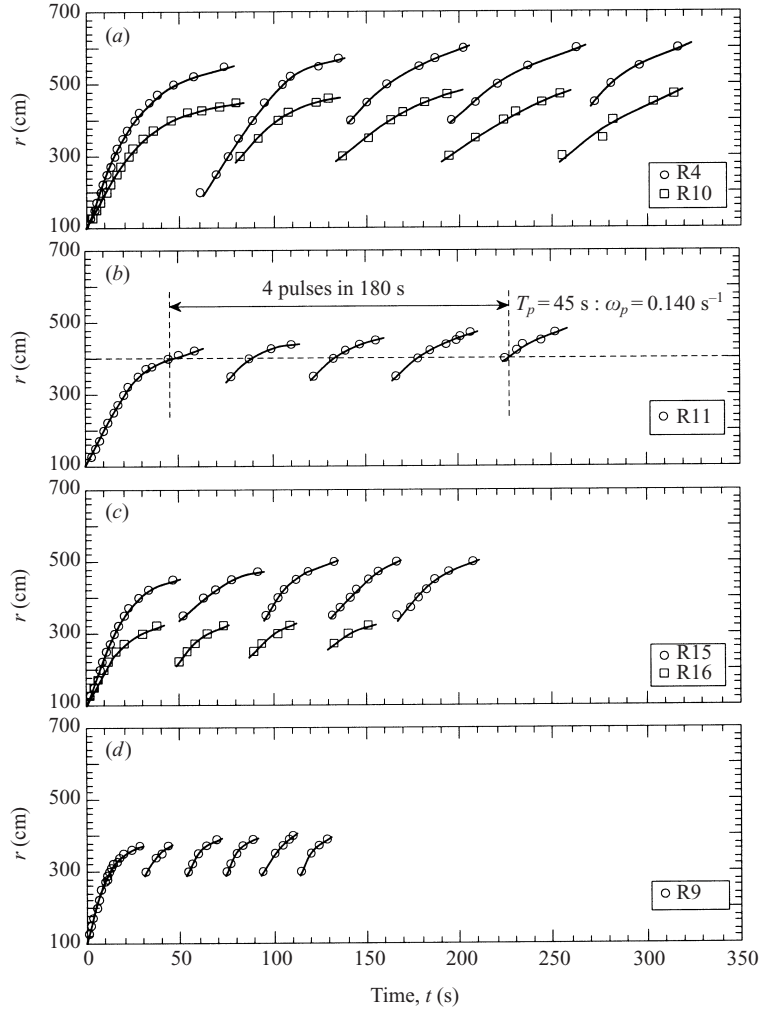


FIGURE 6. The radius of the leading edge of successive outward propagating fronts plotted as a function of time for representative experiments at four different rates of rotation Ω : (a) 0.0500, (b) 0.0641, (c) 0.0775, (d) 0.1500. The determination of the pulse frequency ω_p is shown as an example in (b).

given radius. The pulse frequency ω_p is then defined as

$$\omega_p = \frac{2\pi}{T_p}. \quad (2.20)$$

The experimentally measured values of r_{\max} and ω_p are presented in table 1. In figure 7, the measured pulse frequency is plotted against the rotation rate for each run. A linear relationship is observed of the form

$$\omega_p = c\Omega, \quad (2.21)$$

with the best-fit straight line through the data yielding a value of $c = 2.10$. It is also evident that this relationship appears to be completely independent of the initial values of h_0 and g' . The conclusion is that these pulses are a manifestation of the inertial oscillations in rotating fluids, whose inviscid frequency is 2Ω . Holford (1994)

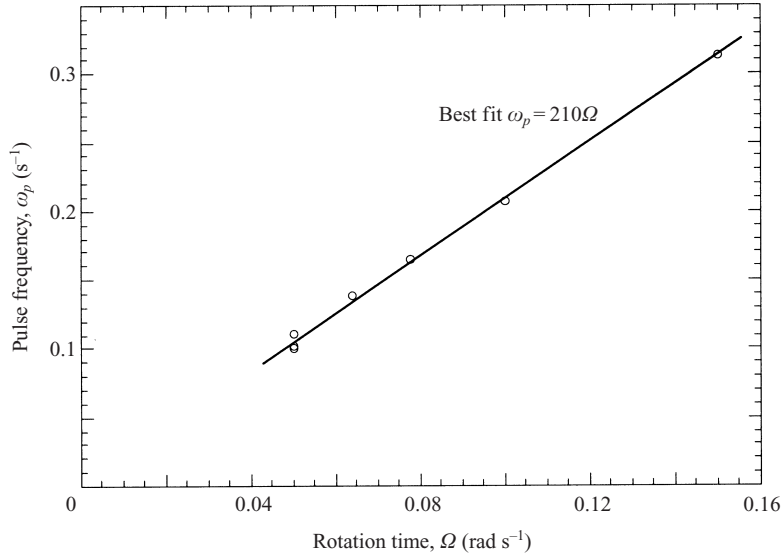


FIGURE 7. The experimentally measured pulse frequency as a function of the rotation rate.

performed experiments on the process of lock-release formation of a steady lens for large \mathcal{C} , see (1.15), and recorded oscillations of the interface of frequency 1.9Ω and of relatively small amplitude. In contrast, the amplitude here is large, about one half the maximal radius. However, the more precise nature of these pulses could not be well understood from the experimental observation. The full numerical solution discussed below suggests that after the contraction of the current, a ring of fluid separates from the bulk, forms a new head, and propagates again. This may be a manifestation of the wave breaking, suggested by Killworth (1992) as an essential mechanism for energy reduction between the initial state and the final steady lens – but this topic was not pursued here.

3. Navier–Stokes numerical simulations

3.1. Formulation

We use the rotating coordinate system defined in §1, and introduce the density function $\phi(\mathbf{r}, t)$ by

$$\rho(\mathbf{r}, t) = \rho_a[1 + \epsilon\phi(\mathbf{r}, t)], \quad (3.1)$$

where ϵ is the reduced density difference defined by (1.2). We expect $0 \leq \phi \leq 1$, with $\phi = 1$ in the ‘pure’ dense fluid domain and $\phi = 0$ in the ‘pure’ ambient fluid domain.

We employ the following dimensionless balance equations:

(i) continuity of volume

$$\nabla \cdot \mathbf{v} = 0; \quad (3.2)$$

(ii) momentum balance

$$\frac{D\mathbf{v}}{Dt} + 2\mathcal{C}\hat{\mathbf{z}} \times \mathbf{v} = \frac{1}{1 + \epsilon\phi} \left[-\nabla p + \phi(\epsilon\mathcal{C}^2 r\hat{\mathbf{r}} - \mathcal{F}^2 \hat{\mathbf{z}}) + \frac{1}{Re} \nabla^2 \mathbf{v} \right], \quad (3.3)$$

where p is the reduced pressure (in dimensional form, $p = P - \rho_a(0.5\Omega^2 r^2 - gz)$);

(iii) density transport

$$\frac{\partial \phi}{\partial t} + \nabla \cdot \mathbf{v}\phi = \mathcal{D}\nabla^2 \phi. \quad (3.4)$$

The relevant dimensionless parameters, in addition to ϵ , are the Reynolds number,

$$Re = UL/v; \quad (3.5)$$

the Coriolis to inertia ratio parameter

$$\mathcal{C} = \Omega L/U; \quad (3.6)$$

the global Froude number squared

$$\mathcal{F}^2 = g'L/U^2; \quad (3.7)$$

and the dimensionless diffusion coefficient $\mathcal{D} = 1/Pe = 1/(\sigma Re)$ where Pe and σ are the Péclet and Schmidt numbers and g' is the reduced gravity defined by (1.1). Here L and U are the scaling length and velocity. Unless specified to the contrary, we employ $L = r_0$ (the dimensional radius of the lock) and $U = (g'r_0)^{1/2}$ and hence $\mathcal{F} = 1$. The scale for time is L/U .

We are interested in flows with large values of Re , moderately small \mathcal{C} , small ϵ and very small \mathcal{D} . Actually, the typical physical value of \mathcal{D} is negligibly small (recall that $\sigma \gg 1$ for saline solutions in water), but here a non-vanishing \mathcal{D} is used as an artificial diffusion coefficient for numerical smoothing of the large density gradients of the moving interface.

The Ekman number can be defined in terms of the previous parameters by

$$E = v/(\Omega L^2) = (\mathcal{C} Re)^{-1} \quad (3.8)$$

and is a small number.

In the considered axially symmetric, lock-release problem in a bounded tank open to the atmosphere, three geometric parameters (in addition to r_0 which is the reference length) appear: the height of the lock, h_0 ; the height of the ambient fluid, H ; and the outer radius of the container, r_w .

The initial conditions at $t = 0$ are

$$\mathbf{v} = \mathbf{0} \quad (0 \leq r \leq r_w, \quad 0 \leq z \leq H), \quad (3.9)$$

$$\phi = \begin{cases} 1 & (0 \leq r \leq 1, 0 \leq z \leq h_0) \\ 0 & \text{elsewhere.} \end{cases} \quad (3.10)$$

The boundary conditions for $t \geq 0$ are

$$\mathbf{v} = \mathbf{0} \quad (\text{on the bottom and sidewalls}); \quad (3.11)$$

$$\mathbf{v} \cdot \hat{\mathbf{z}} = 0, \quad \text{no tangential stress, } p = 0 \quad (\text{on } z = H); \quad (3.12)$$

$$\text{no stress} \quad (\text{on the axis } r = 0); \quad (3.13)$$

and

$$\hat{\mathbf{n}} \cdot \nabla \phi = 0 \quad (\text{on all boundaries}). \quad (3.14)$$

These conditions contain some simplifications. The initial interfaces (between the ambient and dense fluids and also the free surface) deviate from the horizontal by an amount $0.5\epsilon\mathcal{C}^2r^2$, cf. (2.19). The free surface may have an additional height perturbation of magnitude ϵ during the flow. Neglecting these deviations from the horizontal is justified for the small values of ϵ and \mathcal{C}^2 used in the calculations. In addition, we assume that the lock is removed instantaneously and without any perturbation to the fluid. (In experiments the lock lifting takes typically about one dimensionless time unit and introduces a small delay in the initial motion.)

We note in passing the fact that the SW model can be regarded as a solution of the foregoing equations with $\epsilon = Re^{-1} = \mathcal{D} = H^{-1} = 0$, and under the assumption that $\mathbf{v} = \mathbf{0}$ and $\phi = 0$ outside the domain $0 \leq r \leq r_N$, $0 \leq z \leq h(r, t)$, while inside this domain $\phi = 1$ and $[u, v] = [\mathcal{U}(r, t), \mathcal{V}(r, t)]$, and the left-hand side of the axial momentum equation is negligibly small. The scaling here is, for numerical convenience, slightly different from the more insightful one which was used for the SW formulation in § 1.1, and in particular $Re = (r_0/h_0)^{3/2} Re_0$ and $\mathcal{C} = (h_0/r_0)^{1/2} \bar{\mathcal{C}}$.

3.2. The finite-difference code

Consider the time advance of a flow field variable denoted by f at time t to the new value denoted f^+ at time $t + \delta t$. We use a forward-time, finite-difference technique. One time step for the momentum equation (3.3) with the Coriolis and pressure terms treated implicitly and other terms treated explicitly yields

$$\mathbf{v}^+ + 2\mathcal{C}\delta t \hat{\mathbf{z}} \times \mathbf{v}^+ = -\frac{\delta t}{1 + \epsilon\phi} \nabla p^+ + \delta t \mathbf{X} + \mathbf{v} \equiv \mathbf{B}, \quad (3.15)$$

where

$$\mathbf{X} = -\mathbf{v} \cdot \nabla \mathbf{v} + \frac{1}{1 + \epsilon\phi} \left[(\epsilon \mathcal{C}^2 r \hat{\mathbf{r}} - \mathcal{F}^2 \hat{\mathbf{z}}) \phi + \frac{1}{Re} \nabla^2 \mathbf{v} \right]. \quad (3.16)$$

With some simple vector algebra manipulations (as discussed in detail by Ungarish 1993, p. 303), we obtain from (3.15) an explicit expression for \mathbf{v}^+ ,

$$\mathbf{v}^+ = \frac{1}{1 + 4\mathcal{C}^2 \delta t^2} [\mathbf{B} + 4\mathcal{C}^2 \delta t^2 (\hat{\mathbf{z}} \cdot \mathbf{B}) \hat{\mathbf{z}} - 2\mathcal{C} \delta t \hat{\mathbf{z}} \times \mathbf{B}]. \quad (3.17)$$

We next apply the divergence operator to both sides of this expression and impose the continuity equation (3.2) on \mathbf{v}^+ . The result is an elliptic equation for the pressure p^+ at $t + \delta t$,

$$\begin{aligned} \nabla \cdot \frac{1}{1 + \epsilon\phi} \nabla p^+ + 4\delta t^2 \mathcal{C}^2 \frac{\partial}{\partial z} \frac{1}{1 + \epsilon\phi} \frac{\partial p^+}{\partial z} - \nabla \cdot \mathbf{X} - 4\delta t^2 \mathcal{C}^2 \frac{\partial}{\partial z} \hat{\mathbf{z}} \cdot \mathbf{X} \\ - 2\delta t \mathcal{C} \hat{\mathbf{z}} \cdot \nabla \times \mathbf{X} - 4\delta t \mathcal{C}^2 \frac{\partial w}{\partial z} - 2\mathcal{C} \hat{\mathbf{z}} \cdot \nabla \times \mathbf{v} - \frac{\nabla \cdot \mathbf{v}}{\delta t} = 0. \end{aligned} \quad (3.18)$$

(Theoretically the last term on the left is zero, but to prevent accumulation of numerical errors it is sometimes useful to keep it in the calculations.) The boundary conditions for (3.18) are of mixed type: $p = 0$ on the free surface $z = H$, $\partial p / \partial r = 0$ at $r = 0$, and $\hat{\mathbf{n}} \cdot \nabla p^+$ provided by the substitution of (3.11) into (3.15). Hence the solution p^+ is well defined. Using it, we can straightforwardly obtain the velocity field \mathbf{v}^+ from (3.17). The ϕ^+ field can be calculated next using the scalar equation (3.4). This completes, in principle, the time step advance, and a new cycle can be attempted. The accuracy of the time discretization is $O(\delta t^2)$.

The spatial discretization is performed on a staggered grid with il radial intervals and jl axial intervals as sketched in figure 8. The variables p and ϕ are defined at mid-cell position denoted (i, j) ; u and v are both defined at the positions $(i \pm \frac{1}{2}, j)$ (to allow straightforward implementation of the Coriolis coupling) and w is defined at $(i, j \pm \frac{1}{2})$. Both the r and z grid coordinates are stretched by simple mapping functions $r(R)$ and $z(Z)$. The grids $R_i = (i + \frac{1}{2})\delta R$ and $Z_j = (j + \frac{1}{2})\delta Z$ are uniform in the domain ($0 \leq R \leq r_w$, $0 \leq Z \leq H$) with intervals $\delta R = r_w/il$, and $\delta Z = H/jl$. The truncation error is $O(\delta R^2 + \delta Z^2)$. Dummy cells are added for easy implementation of the boundary conditions. An illustration of the finite-difference approximation

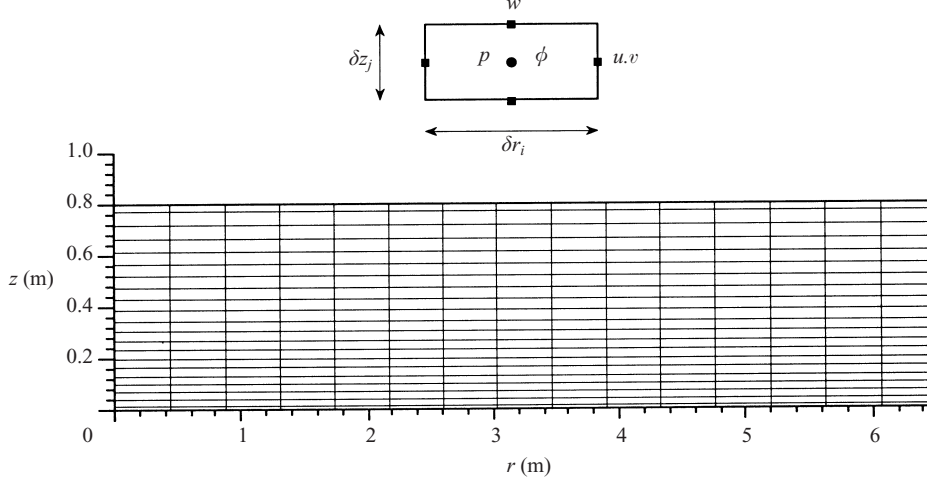


FIGURE 8. The numerical grid, and the details of one cell. The centre of the computational cell is denoted by (i, j) , corresponding to the position r_i, z_j , ($1 \leq i \leq il$, $1 \leq j \leq jl$).

approach is

$$\left(\frac{1}{r} \frac{\partial}{\partial r} r \frac{1}{1 + \epsilon \phi} \frac{\partial p}{\partial r} \right)_{r_i, z_j} \approx \frac{1}{r_i} \frac{1}{r'_i \delta R} (Y_{i+1/2, j} - Y_{i-1/2, j}), \quad (3.19)$$

where

$$Y_{i+1/2, j} = r_{i+1/2} \frac{1}{1 + \epsilon \phi_{i+1/2, j}} \frac{1}{r'_{i+1/2} \delta R} (p_{i+1, j} - p_{i, j}) \quad (3.20)$$

and r'_i is the derivative of $r(R)$ at R_i (substituting $i - 1$ in place of i yields $Y_{i-1/2, j}$).

This method of central differences was employed for all terms, except for the advection terms in the ϕ transport equation (3.4). For this equation, according to MacCormack's explicit method, we used at each time step the predictor–corrector relationships

$$\left. \begin{aligned} \phi_{i, j}^p &= \phi_{i, j} - \delta t (Adv_f \phi^f)_{i, j} + \delta t (Dif \phi)_{i, j}, \\ \phi_{i, j}^c &= \phi_{i, j}^p - \delta t (Adv_b \phi^p)_{i, j} + \delta t (Dif \phi^p)_{i, j}, \\ \phi_{i, j}^+ &= 0.5(\phi_{i, j} + \phi_{i, j}^c), \end{aligned} \right\} \quad (3.21)$$

where Adv_f and Adv_b denote the advection terms as approximated by forward and backward differencing, and Dif denotes the diffusion terms approximated by central differences.

The combination of the foregoing time and space discretizations is the core of the computer code used in this work. For each time step the discretized form of the Poisson equation (3.18) for the discretized variables $p_{i, j}^+$, $1 \leq i \leq il$, $1 \leq j \leq jl$, must be solved. This yields, after the implementation of the boundary conditions, a block tri-diagonal linear system.† The matrix corresponding directly to (3.18) is non-symmetric, but upon multiplication of each of the discretized equations for point

† The straightforward numerical implementation of the previously defined ‘open boundary’ condition introduces an $O(1/Re)$ inconsistency in the continuity equation on the interface; however, since the velocities there are very small, the influence of this numerical error on the motion of the current is insignificant. This has been numerically verified by tests with a rigid inviscid lid condition (and $p = 0$ applied at some computational point instead of on the interface).

(i, j) by $r_i r'_i z'_j$ a symmetric system can be obtained (in our computation there was no noticeable difference between the performances of these versions). The linear system was solved by a bi-conjugate gradient iterative algorithm (Press *et al.* 1992). The iterations in the first time step start with 0, and subsequently the $p_{i,j}$ field provides the starting values for $p_{i,j}^+$. Some test cases were also run with a direct solver for the block tri-diagonal system. The computations use real-8 variables. The typical grid has $il = 175$ constant radial intervals and $jl = 240$ stretched axial intervals, with $z'_1 \approx 0.7$ and $z'_{jl} \approx 1.4$; this was motivated by a compromise between computational limitations and physical considerations, as discussed further below. The typical time step was $\delta t = 10^{-3}$. In several test cases the grid size was changed and the time step was halved, without causing any significant differences in the results. The diffusion coefficient in the density transport equation was usually taken as $\mathcal{D} = 0.3\delta R^2$ and $\mathcal{D} = 0.3\delta Z^2$ for the radial and axial fluxes, respectively, and hence this artificially augmented effect is expected to be of the order of magnitude of the numerical truncation error in the physical advection term.

The bi-conjugate gradient method performed typically 200 iterations per time step to reach the allowed error $e = 10^{-4}$, where e is the Euclidean seminorm of the residues divided by the seminorm of the right-hand side of the system of equations. The typical average relative error, $e/(il \times jl)$, in the solution of $p_{i,j}^+$ is therefore less than 10^{-8} .

The choice of the numerical grid parameters was motivated by a compromise between physical accuracy considerations, see below, and computational limitations. Essentially, the mesh intervals are considerably smaller than the expected typical corresponding geometrical dimensions of the simulated current, such as the length of the ‘head’, the average thickness, and even the Ekman layer thickness (estimated as $3E^{1/2}$). Nominally, the magnitude of the spatial errors $\delta R^2 + \delta Z^2$ is less than 0.2%, and of the accumulated time-stepping errors $N\delta t^2$ (where N is the number of time steps) is also typically less than 0.2%; the value of $\delta R^4 + \delta Z^4$ which typifies the smoothing dissipation terms (see below) is about 10^{-6} , smaller than $1/Re$. We therefore expect that the numerical results provide an acceptable simulation of an observable gravity-current process, at least during the initial period. Eventually, when the current becomes thin (say, about 10 axial intervals) and the interface very irregular, the numerical errors may become significant and even dominant.

In some cases we also encountered a practical numerical restriction on the time interval, t , for which results could be obtained which is due, apparently, to a nonlinear instability which appears after some development of the flow. Typically—but not always—for $t \approx 5$, some spurious oscillations appeared, the linear system for $p_{i,j}$ became almost singular and it was necessary to stop the computation. The addition of small $O(\delta r^4 + \delta z^4)$ fourth-order derivative dissipation terms in the momentum equations improved the stability. However, as the major remedy we used an artificial higher value of viscosity, simply by the artificial reduction of the Reynolds number, typically by a factor of ten (which still leaves the Reynolds number large so that the essentials of the flow field are well reproduced).

The numerical code has also been tested on several other problems. Computations of spin-up (differential and from rest) of homogeneous, two-layer, and stratified fluids yielded good agreement with independent theoretical and experimental results. Simulations of gravity currents in a rectangular (two-dimensional) geometry showed good agreement with SW approximations. These results will be reported elsewhere.

The task discussed here was to simulate the rotating current for the time interval $t \approx 2\mathcal{C}^{-1}$ (in dimensional form, $\Omega t \approx 2$), during which the most significant effects of propagation and attainment of maximal spread are expected to take place.

Label	r_0 (cm)	h_0 (cm)	H (cm)	Ω (s ⁻¹)	\mathcal{C}^2	$\bar{\mathcal{C}}^2$	g' (cm s ⁻²)	Re ($\times 10^5$)
S3	100	45.8	79.8	0	0	0	19.2	4.3
R5	100	46.3	79.8	0.100	0.0526	0.114	19.03	4.3
R14	100	44.0	81.1	0.05	0.0257	0.059	9.72	3.1
R16	100	16.7	83.3	0.078	0.0251	0.150	23.94	5.0
VIR-1	100	46.3	79.8	0.594	1.86	4.000	19.03	4.3

TABLE 2. Data of configurations in the numerical simulations. For S3, R5 and VIR-1 the value of Re was reduced by a factor of 10.

3.3. Results of Navier–Stokes numerical simulations (NS)

Table 2 summarizes the configurations for which numerical simulations were carried out. These configurations were motivated by the measurements performed at the Coriolis laboratory and the labels refer to the corresponding experiments discussed in the previous sections. VIR-1 is an exception, a ‘virtual experiment’ with a value of Ω larger than allowed on the present turntable; this case with large \mathcal{C} has been added as a contrast to the other runs with small \mathcal{C} , as an additional test of the predictive power of the numerical code and the SW approximation.

Consider in detail the configurations labelled R5 and S3 in table 2. The difference between the cases is the presence of rotation in the case R5. The reference time, $(r_0/g')^{1/2}$, is 2.3 s and the period of revolution in R5 is 62.8 s. Note that the initial fractional depth $h_0/H = 0.57$ in both cases.

The numerical grid had typically 175×240 intervals. In dimensional form, the radial grid intervals were of uniform size $\delta r = 3.7$ cm, judged as acceptable because the typical length of the observed ‘head’ was about 20 cm, and the estimated experimental error of its position is estimated as about 3–5 cm (the tank floor marks were at 10 cm intervals, see figure 2). The dimensional axial grid intervals changed from $\delta z = 0.26$ cm near the bottom to $\delta z = 0.47$ cm near the top free boundary; this is expected to provide a fair description of the thinning current during a considerable spread (the average thickness is about 4 cm when the container middle radius 3.25 m is reached at $t \sim 20$ s) and of the Ekman layer (whose thickness for water with $\Omega = 0.1$ s⁻¹ is approximately 1 cm). The run with the correct Re diverged at about $t = 18$ s, and with a 10 times larger artificial viscosity $t = 40$ s was reached.

Figure 9 displays contour plots of the numerically computed density function, ϕ , for two representative gravity currents, the non-rotating S3 and the rotating R5 cases. Also shown are the SW results for the interface $h(r)$ (in the rotating case this approximation can be used for a limited time interval, until the height of the nose decays to zero). Figure 10 displays the behaviour of the radius of propagation, $r_N(t)$ obtained by the SW approximation, NS and experiments for these cases.

It is evident that the numerical code captures well the propagation of the current and the differences between the rotating and the non-rotating cases.

The numerical results point out the very complicated shape of the interface of the current, which is very different from the usually smooth $h(r, t)$ provided by the SW approximation. In the rotating case after $t = 14$ s ($\Omega t = 1.4$) while the head spreads and becomes less and less prominent, a complex re-arrangement of the fluid in the tail occurs, which includes contraction toward the centre ($t = 28$ s) followed by a forward pulse.

The rotating current evidently reaches a maximum radius of propagation at $t \approx 28$ s

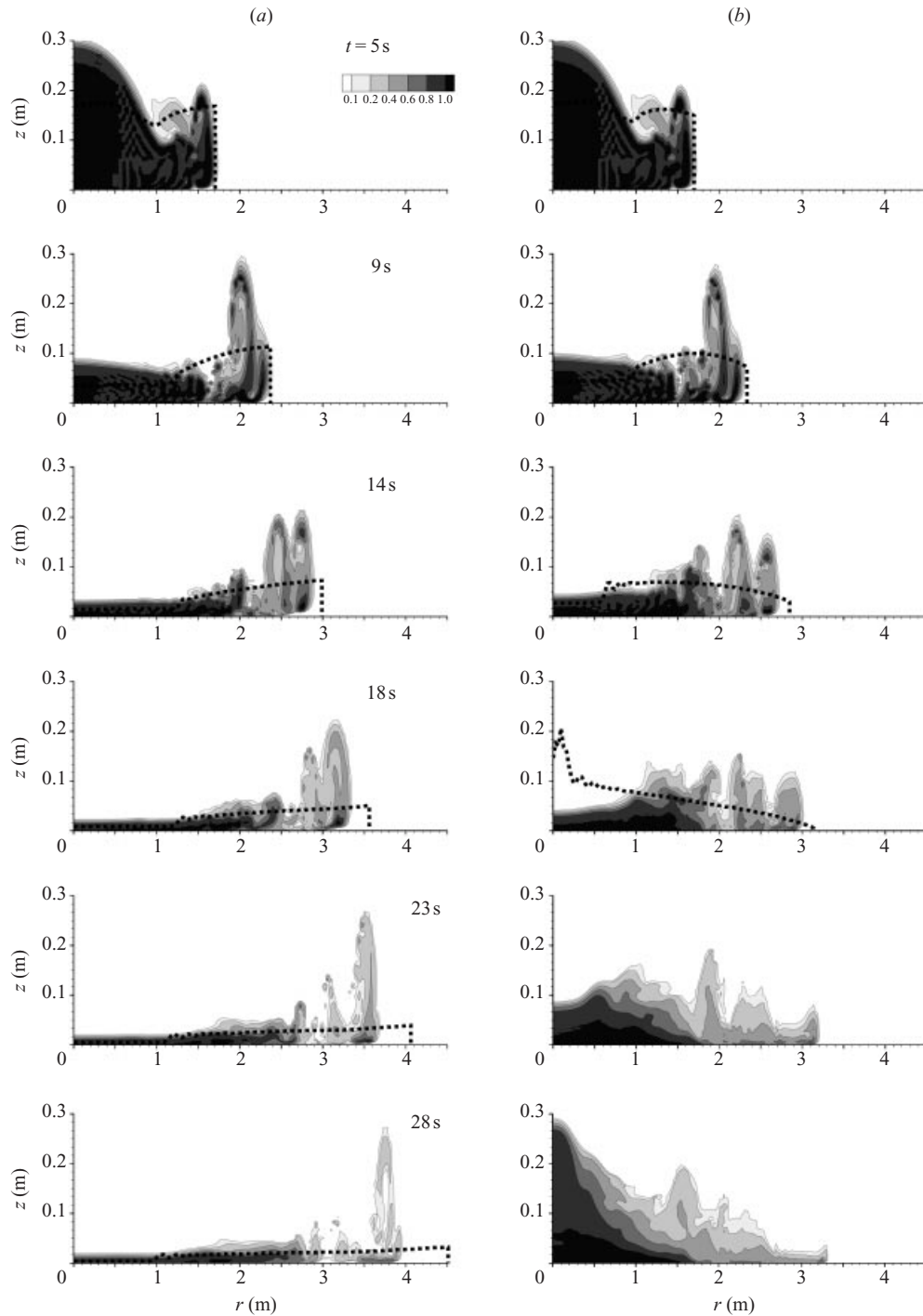


FIGURE 9. The NS results for the density function (contour lines and shading) and the SW results for the interface $h(r)$ (dashed lines), at various times, for cases S3 (a) and R5 (b).

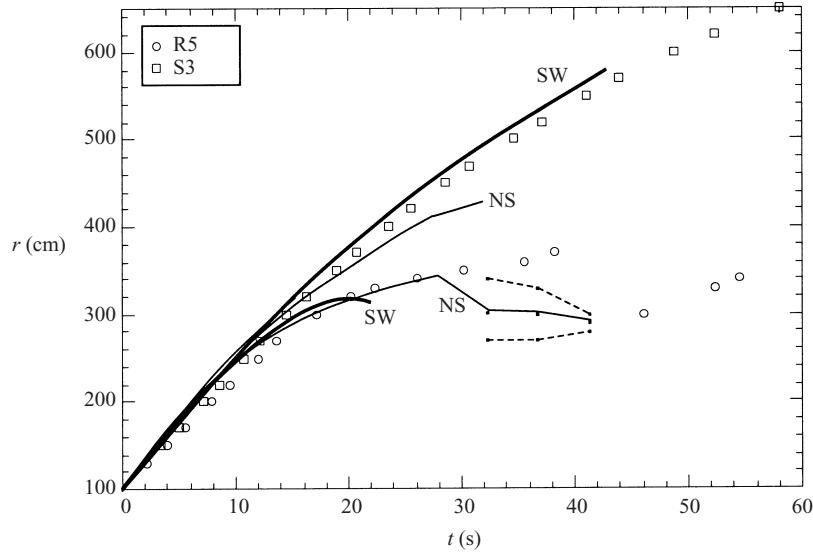


FIGURE 10. The radius of propagation as a function of time for experiments S3 and R5, compared with the corresponding NS and SW predictions. The dotted lines in the numerical R5 results indicate the thin spread of the head.

($\Omega t = 2.8$, about 0.45 revolutions of the system). Afterwards, the position of $r_N(t)$ is not well defined because there is no clear ‘head’. For instance, at $t = 32$ s the bulk of the heavy fluid is in the domain $0 < r < 2.6$ m, but there is also a very thin residual layer extending up to $r = 3.4$ m. The interpretation of this layer is not clear. It may be just a numerical artifact due to lack of resolution, but it may also indicate (although with very low accuracy) the physical tendency of a thin viscous layer to stick to the wall. We note in this context that a quite similar qualitative behaviour was observed in the experiments: after the front of the dyed fluid reaches a clear maximum, its position becomes eventually more ambiguous and the bulk of fluid apparently contracts to a smaller radius, leaving behind a residue of faint colour (probably a thin layer).

In the numerical computations of R5 a new ‘head’ of fluid separated from the bulk and started to propagate freely at $t = 37$ s (not shown). We tend to identify the propagation of this new head with the first of the outwardly propagating pulses, with a clearly defined leading edge, observed in the experiment. Indeed, in the experiment such a pulse has been detected at $t \approx 45$ s at $r \approx 300$ cm.

Comparison between S3 and R5 at $t = 23$ s shows clearly that in the non-rotating case, unlike the rotating one, the head region becomes the most prominent feature of the current; obviously, the distance of propagation is also larger. This is in good qualitative agreement with the SW approximation which predicts that the Coriolis effects modify the profile from ‘nose up’ to a ‘nose down’ shape after about the first tenth of a revolution.

Figure 11 shows the vector plot of the velocity in the (r, z) -plane for R5. Evidently, at $t = 18$ s the motion in the main bulk of the current, $r < 2.7$ m, is toward the centre. The head region displays a more complex rolling motion in the counter-clockwise direction. No such motion appears in the non-rotating current.

Consider next the angular velocity field of R5, figure 12. The measurement of angular velocity inside the propagating current is an extremely difficult task and

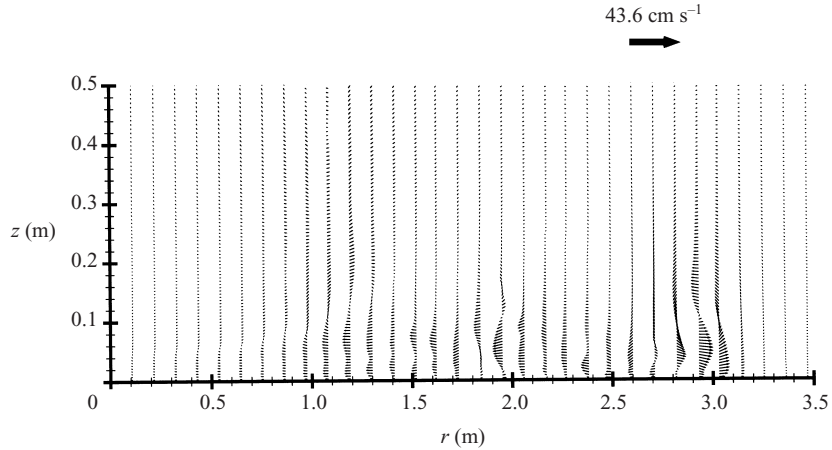


FIGURE 11. NS results of meridional velocity field for R5 at $t = 18$ s. (The unit reference vector is also displayed.)

has never been performed in laboratory experiments, to our best knowledge. The numerical experiments, on the other hand, provide this information as a standard part of the solution. We observe that the dense-fluid current has a very distinct ‘signature’ as a region of strong counter-rotation (relative to the rotating system). This, again, is in good qualitative agreement with the SW z -averaged approximation, but the NS provide, as expected, more details.

A comparison between results with the present artificial value of Re and with the correct value (ten times smaller) was also performed for $t < 15$ s. We found that the larger artificial viscosity causes a reduction in the distance of propagation $r_N(t)$, as could be expected, but actually the difference is very small. The other details of the flow field are also very close. The $r_N(t)$ predicted by the inviscid, SW equations is in excellent agreement with the calculations with the original Re . The experimental r_N lags behind the theoretically determined results for $t < 15$ s, an effect which we attribute to the non-ideal lifting of the lock.

We think that the various behaviours and effects of the computed flow fields R5 and S3, as well as the agreements with the experiments and SW results, provide a good validation of our numerical approach. The blurred and even patchy profiles obtained in the NS, which are very different from the sharp SW predictions, may raise doubts about the reliability of the numerical solution. However, we think that this shape indeed reflects the non-smooth behaviour of a real gravity current. This is illustrated by the experiment R14, in which we used fluorescein and a laser sheet to visualise the (r, z) shape. Some video records are shown in figure 13 and compared with numerical results. The impression is that not only the position of the front, but also the shape of the head are in fair agreement. In particular, we notice that both the experiment and the computations show that the maximum height of the head increased by about 5 cm from $t = 10$ s to 16 s. A detailed comparison is not possible because we have no measurements of the concentration of salt and fluorescein.

Additional results of interest are obtained from the simulation corresponding to the experiment R16 in table 2, see figures 14 and 15. In this case the current is initially ‘deep’, $h_0/H = 0.2$, in contrast with the previously discussed cases, S3 and R5, where this ratio was 0.57. The shallower current R16 is expected to be slower than R5. Furthermore, the parameter \mathcal{C} of R16 is larger than the one of R5 and hence a

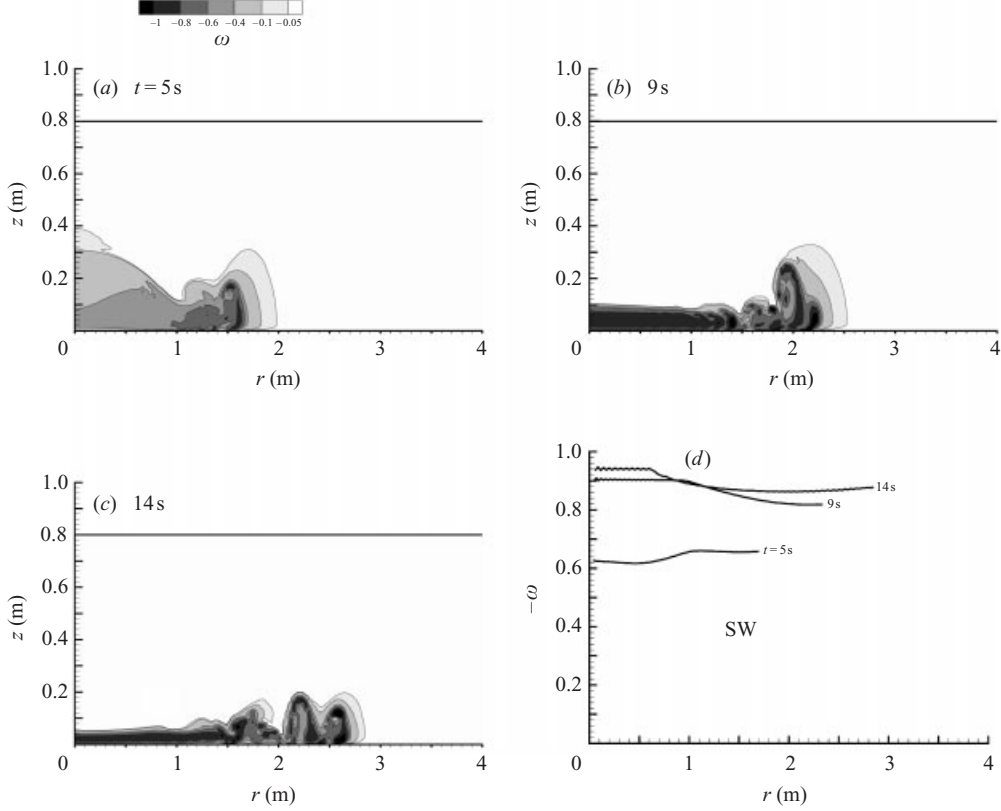


FIGURE 12. The angular velocity for R5 at various times (a–c): NS results (field contours) and (d) SW results (in the dense fluid).

stronger Coriolis hindering on R16 is also expected. The reference time, $(r_0/g')^{1/2}$, is 2.04 s and the period of revolution is 81 s.

We observe excellent agreement between the experimental and numerical results for $r_N(t)$ up to $t \approx 25$ s. (At this time the maximal expansion is achieved according to both the SW and NS results.) The SW predicts a more rapid motion than the NS. These trends are different from those observed in other cases, namely that there is a good agreement between the SW and NS, and both are more rapid than the experiment. The explanation is as follows. Since h_0 in the present case is small the current is little affected by the lock removal delay, and is therefore more compatible with the ideal lock removal in the NS. This justifies the better than usual agreement between NS and experimental values of $r_N(t)$. On the other hand, this configuration is more affected by Coriolis effects and viscous friction than usual, because $\bar{\mathcal{C}}^2 = 0.15$, not so small, and the current is thin and hence more influenced by the Ekman layers (when the current is expanded to 250 cm its average thickness is 2.7 cm, while $3(\nu/\Omega)^{1/2} = 1.1$ cm). This explains the faster motion of the SW approximation, in which the nose Froude condition does not take into account Coriolis hindering (UH estimated this contribution as $O(\bar{\mathcal{C}}^2)$) and viscous effects are also discarded. Indeed, we found that at $t = 22$ s the computed current displays a coherent negative $\omega = v/r$ profile, but at $t = 33$ s much of the azimuthal lag has dissipated.

We observe again that when the current is close to the maximum radius of propagation ($t = 20$ s) the nose region detaches from the body of the current. The

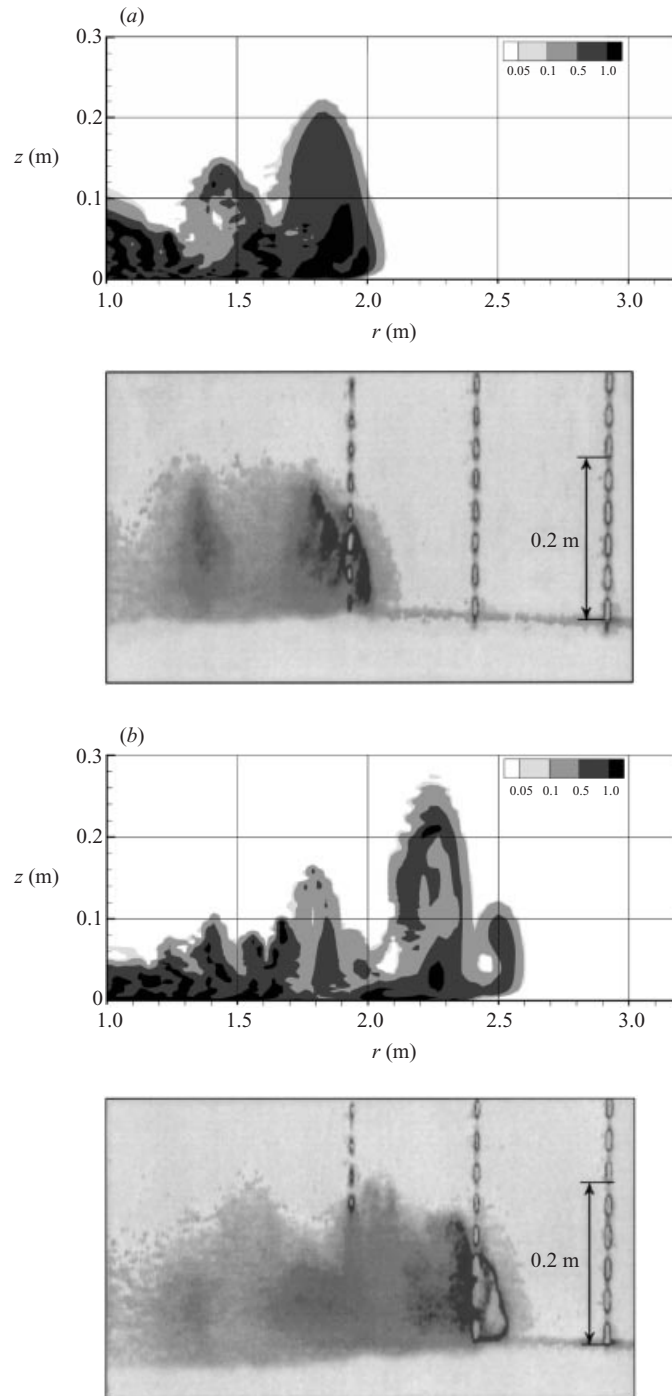


FIGURE 13. Experimental and numerical r, z profile for R14 at (a) $t \approx 10$ s and (b) 16 s.

latter remains roughly in the domain $0 \leq r \leq 250$ cm where, again, some contraction–expansion pulses appear. The second maximum of propagation is attained about 37 s after the first one, which suggests that the frequency of this occurrence is $0.17 \text{ s}^{-1} \approx 2.2\Omega$, in agreement with the experimental observations.

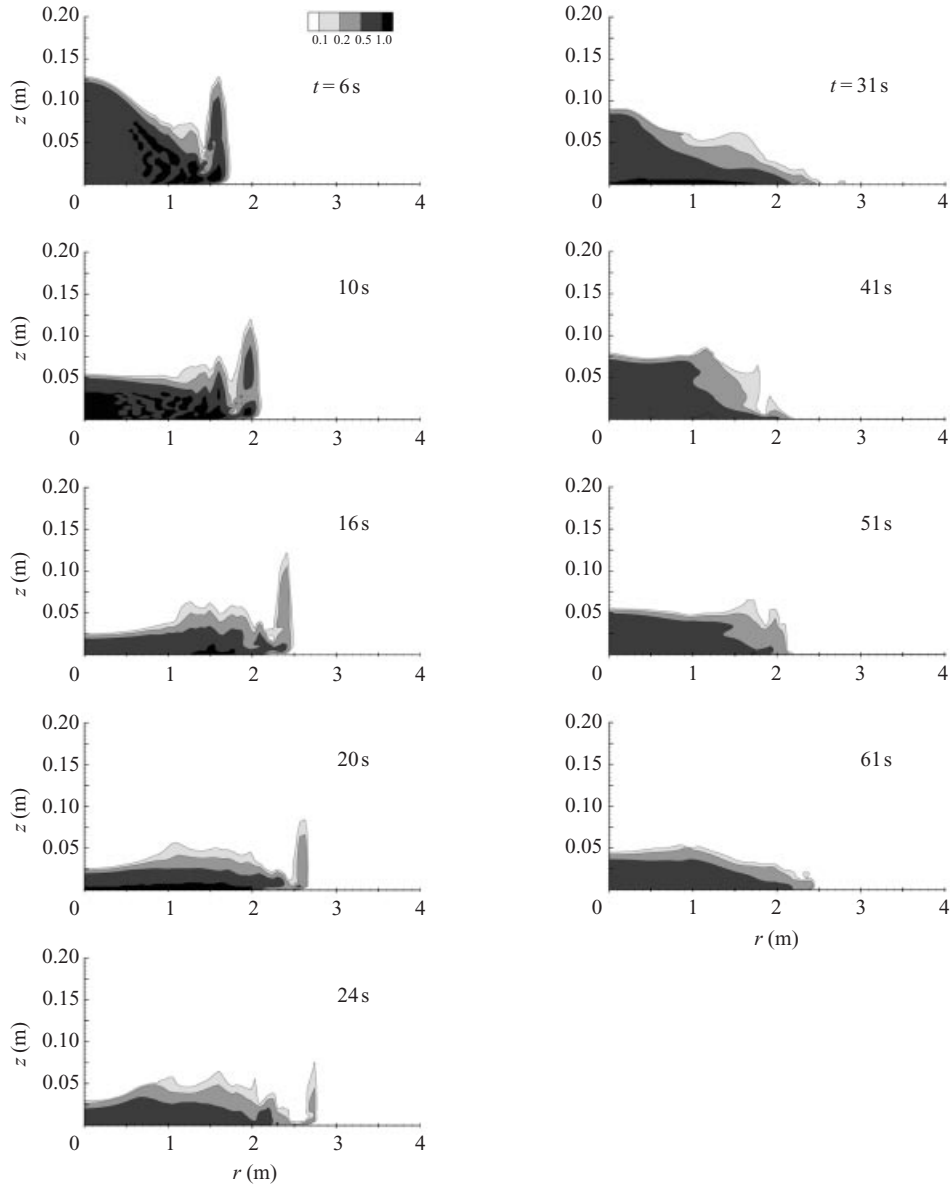


FIGURE 14. The NS results for the density function (contour lines and shading), at various times, for case R16 ($\Omega t = 0.50, 0.80, 1.3, 1.6, 1.9, 2.4, 3.2, 4.0, 4.8$).

Another feature of interest is the somewhat more compact structure of the interface in R16. Observations on non-rotating currents indicate that a ‘multiple-front’ structure appears when the initial depth ratio h_0/H is greater than 0.5 (approximately), as in cases S3 and R5, and a ‘single-front’ structure appears otherwise, as in case R16. This influence of h_0/H seems to apply also to the rotating current, which suggests that this structure of the interface is determined by the early stage of propagation, when the Coriolis effects are still unimportant. This topic will be investigated elsewhere.

Finally, we consider the simulation labelled VIR-1 for the case with a large value of the Coriolis influence parameter, $\mathcal{C} = 2$ (a small Rossby number). We use the

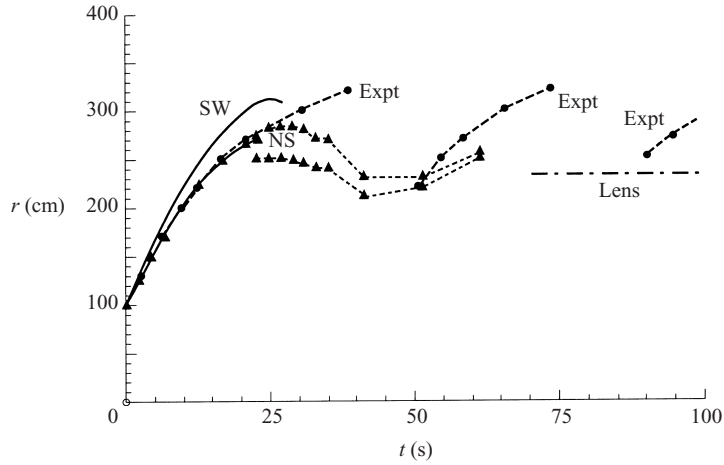


FIGURE 15. The radius of propagation as a function of time for experiment R16, compared with the corresponding NS and SW predictions. The dotted lines in the numerical results indicate the thin spread of the head. The radius of the theoretical steady lens is also shown.

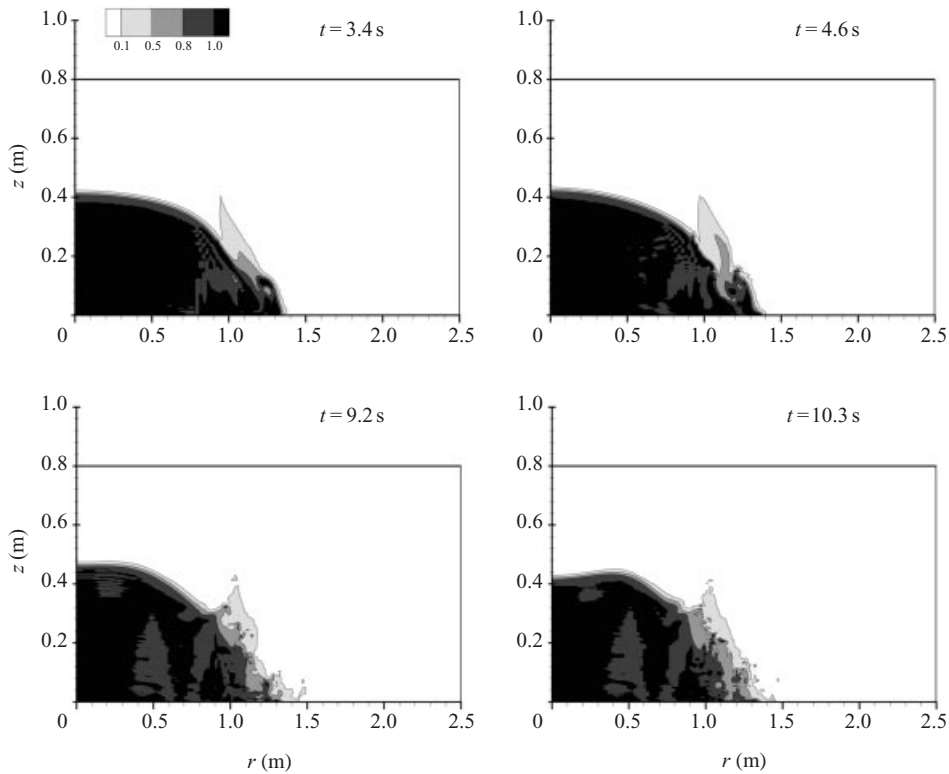


FIGURE 16. NS results for the density function at various times, case VIR-1 ($\Omega t = 2.0, 4.1, 5.4, 6.1$).

same geometry and fluids as in R5, but with a much larger angular velocity. (This brings us to the parameter range investigated by Holford 1994.) Since a small amount of propagation was expected, the NS was performed with $r_w = 2.5$. Again, artificial higher viscosity was used.

Figure 16 indicates that the numerical code captures well the special features of this case: the Coriolis influence is very strong and therefore the amount of propagation of the current is small. The Rossby radius of deformation in the VIR-1 case is $r_0/2\bar{\mathcal{C}} = 0.25$ cm, and the actual propagation exceeds it by about 30%. The maximum propagation is achieved at about $t = 4.6$ s ($\Omega t = 2.7$), and afterwards a contraction–expansion motion of the lens-shaped bulk, with small oscillations of the interface, appears. Considering the first cycle of vertical displacement of the interface at the centre (whose amplitude is 4 cm), we estimated that the period of the oscillation is 6.9 s, i.e. the frequency is about 1.5Ω . All this numerically simulated behaviour is consistent with the experimental observations of Holford (1994, §3.6.2) concerning formation of lenses with large $\bar{\mathcal{C}}$. The angular velocity results in the VIR-1 case indicate that significant variations from the initial solid body rotation occur only in the region of the head, as expected. However, the pattern of ω in this region is quite irregular (unlike the smooth steady-lens solution) perhaps due to the influence of the various shear mechanisms which act during the formation of the head.

The propagation of the current by more than one Rossby radius in this case is unlike the small $\bar{\mathcal{C}}$ case where the radius of propagation is smaller than the Rossby radius of adjustment. This is consistent with the analysis of the quasi-steady lens (UH, §3). On the other hand, there are also similarities between the small- $\bar{\mathcal{C}}$ case R16 and large- $\bar{\mathcal{C}}$ case VIR-1 as follows. In both cases the maximum propagation is achieved at about $\Omega t = 2$ (about 0.4 revolution of the system); a physical interpretation of this behaviour is given in the Appendix.

4. Concluding remarks

We investigated the motion of axisymmetric high-Reynolds-number gravity currents produced by the instantaneous release of a cylinder of dense fluid into a less-dense ambient fluid above a horizontal bottom. The system was considered to be at rest or rotating with constant angular velocity. The work combined experiments in a large tank (13 m diameter, with a layer of ambient water of about 80 cm, in which a cylinder of 2 m diameter of salt water was released), with theoretical simulation by: (a) a special-purpose code for finite-difference numerical solution (NS) of the full axisymmetric equations of motion, and (b) the shallow-water (SW) approximate solution developed by UH.

The analysis was focused on small values of the parameter $\bar{\mathcal{C}}$ which represents the ratio of Coriolis to inertia terms. The results reconfirm the significant differences between rotating and non-rotating gravity currents even for small values of this parameter.

The spreading of the current as a function of time was the major experimental result. In all cases, the experimental radius-of-propagation results were in very good agreement with both the full numerical and the SW theoretical predictions for the main period of radial spread. The (rather small) discrepancies can be attributed to the non-ideal release of the dense fluid in the experiment. The conclusion is that in the SW approximation the use of the ‘nose’ Froude condition (1.12)–(1.13) developed for rectangular non-rotating currents is also appropriate for axisymmetric and rotating gravity currents with small $\bar{\mathcal{C}}$.

Moreover, the experiments in the rotating configurations show that the flow field displays large-amplitude oscillations, with a frequency slightly larger than the inertial 2Ω . These oscillations are not captured by the available SW formulation, and, to our best knowledge, have not been reported before for flows with small values of $\bar{\mathcal{C}}$.

On the other hand, the experiments pose certain technical difficulties which limit the obtainable information. The present experiments were expensive and time consuming, restricted by various geometry and angular velocity constraints, and, typically, provided little information about the shape of the interface and velocity field. These problems cannot be easily overcome, and are expected to become more acute when additional effects, such as stratification, are of interest. Therefore, in order to gain reliable information about the above-mentioned properties, it is important to supplement the laboratory experiments with ‘numerical’ counterparts based on the solution of the full governing equations of motion. In this respect we conclude that the present NS code indeed provides a means for useful ‘numerical experiments’. We mention that a numerical computation for a large value of $\bar{\mathcal{C}}$, which is beyond the practical capability of the laboratory device, was also successfully performed. However, due to computational and stability limitations, further numerical improvements and verifications are necessary for making the present numerical computations a versatile tool of simulation and a substitute for laboratory experiments. Still, we must keep in mind that an axisymmetric code imposes on the attainable results limitations which are incompatible with some of the complex features displayed by a real gravity current (such as the formation of lobes and edge instability waves).

The comparison of numerical and experimental results with shallow-water z -averaged results shows significant differences in the details of the flow field: in the numerical results there is not a smooth shape of the interface, the velocities in the current are strongly z -dependent, and there is a strong rolling motion in the head region. In these respects the numerical results seem in fair qualitative agreement with the experiments. We conclude that a great deal of information beyond SW results is needed in the analysis and design of processes in which the details of the internal flow in the current may be of importance.

The clearly detected combination of large-amplitude oscillations (with a frequency slightly larger than the inertial 2Ω) and complex internal motion (rings of fluid seem to break away from the bulk during the expansion–contraction effect) raises doubts about the convergence of the lock-released rotating gravity current to a steady-lens structure, and its stability. In other words, the steady-lens solution of the SW formulation is apparently not a regular limit of the instantaneous lock-release problem (at least when the value of the parameter $\bar{\mathcal{C}}$ is small). This problem is left for a future study.

We thank Dominique Renouard, Henri Didelle, Rene Cartel and Johny Mang for their help with the experimental system at Grenoble. The research was supported by the TMR-EU, EPSRC and by the Fund for Promotion of Research at the Technion.

Appendix. Estimate of time to attain r_{\max}

It is surprising that the value of r_{\max} for the rotating axisymmetric current is attained at $t \sim \Omega^{-1}$ for both mild and strong Coriolis influence, i.e. $\bar{\mathcal{C}} \ll 1$ and $\bar{\mathcal{C}} \gg 1$. The explanation is as follows.

The situation $\bar{\mathcal{C}} \gg 1$ is the simpler case. The steady-lens analysis in UH shows that $r_{\max} - r_0 \approx r_0/2\bar{\mathcal{C}} < r_0$. Thus, r_{\max} is achieved during the initial ‘slumping’ phase of the gravity current, during which the speed of propagation is $U \sim (g'h_0)^{1/2}$. The corresponding $(r_{\max} - r_0)/U$ is $\sim 2/\Omega$.

For the $\bar{\mathcal{C}} \ll 1$ case the steady-lens analysis indicates that $r_{\max} \approx \sqrt{2}r_0/\bar{\mathcal{C}}^{1/2} \gg r_0$. During this considerable spread the current is expected to be mainly in its self-similar

phase, thus

$$r_N(t) \approx 2kr_0^{1/2}(g'h_0)^{1/4}t^{1/2},$$

where $k = [Fr^2/(4 - Fr^2)]^{1/4} \approx 1$ (for $Fr = 1.19$). This similarity-type propagation attains the above value of r_{\max} at $t \sim 2/\Omega$.

These crude considerations underestimate the correct time of propagation to r_{\max} because they do not account for the deceleration introduced by the Coriolis forces. However, the indication that r_{\max} is attained in a time interval $\sim \Omega^{-1}$ for both large and small values of the parameter \mathcal{C} remains valid. Note that the values of \mathcal{C} considered in this paper do not truly lie in the asymptotic ranges of ‘very small’ and ‘very large’ (in table 2, $0.15 \leq \mathcal{C} \leq 2$).

REFERENCES

- BENJAMIN, T. B. 1968 Gravity currents and related phenomena. *J. Fluid Mech.* **31**, 209–248.
- CHOBOTER, P. F. & SWATERS, G. E. 2000 On the baroclinic instability of axisymmetric rotating gravity currents with bottom slope. *J. Fluid Mech.* **408**, 149–177.
- CSANADY, G. T. 1979 The birth and death of a warm core ring. *J. Geophys. Res.* **84**, 777–780.
- FLIERL, G. R. 1979 A simple model for the structure of warm and cold core rings. *J. Geophys. Res.* **84**, 781–785.
- GRIFFITHS, R. W. & LINDEN P. F. 1981 The stability of vortices in a rotating, stratified fluid. *J. Fluid Mech.* **105**, 283–316.
- HALLWORTH, M. A., HUPPERT, H. E., PHILLIPS, J. C. & SPARKS, R. S. J. 1996 Entrainment into two-dimensional and axisymmetric turbulent gravity currents. *J. Fluid Mech.* **308**, 289–311.
- HÄRTEL, C., MEIBURG, E. & NECKER, F. 2000 Analysis and direct numerical simulation of the flow at a gravity current head. Part 1. Flow topology and front speed. *J. Fluid Mech.* **418**, 189–212.
- HOGG, A. J., UNGARISH, M. & HUPPERT, H. E. 2001 Axisymmetric gravity currents: asymptotic analysis of the effects of particle-sedimentation and rotation. *Phys. Fluids* (in press).
- HOLFORD, J. M. 1994 The evolution of a front. PhD thesis. University of Cambridge.
- HUPPERT, H. E. & SIMPSON, J. E. 1980 The slumping of gravity currents. *J. Fluid Mech.* **99**, 785–799.
- HUPPERT, H. E. 2000 Geological fluid mechanics. In *Perspectives in Fluid Dynamics: A Collective Introduction to Current Research* (ed. G. K. Batchelor, H. K. Moffatt & M. G. Worster), pp. 447–506. Cambridge University Press.
- HUQ, P. 1996 The role of aspect ratio on entrainment rates of instantaneous, axisymmetric finite volume releases of dense fluid. *J. Hazard. Mat.* **49**, 89–101.
- KILLWORTH, P. D. 1992 The time-dependent collapse of a rotating fluid cylinder. *J. Phys. Oceanogr.* **22**, 390–397.
- PRESS, W. H., TEUKOLSKY, S. A., VETTERLING, W. T. & FLANNERY, B. P. 1992 *Numerical Recipes in Fortran*. Cambridge University Press.
- SIMPSON, J. E. 1997 *Gravity Currents in the Environment and the Laboratory*. Cambridge University Press.
- UNGARISH, M. 1993 *Hydrodynamics of Suspensions*. Springer.
- UNGARISH, M. & HUPPERT E. H. 1998 The effect of rotation on axisymmetric gravity currents. *J. Fluid Mech.* **362**, 17–51 (referred to herein as UH).
- UNGARISH, M. & HUPPERT E. H. 1999 Simple models of Coriolis-influenced axisymmetric particle-driven gravity currents. *Intl J. Multiphase Flow* **362**, 715–737.
- WANG, D.-P. 1985 Numerical study of gravity currents in a channel. *J. Phys. Oceanogr.* **15**, 299–305.